RMetS

Royal Meteorological Society

The response of the Pacific storm track and atmospheric circulation to Kuroshio Extension variability

Christopher H. O'Reilly* and Arnaud Czaja

Department of Physics, Imperial College London, UK

*Correspondence to: C. H. O'Reilly, Faculty of Science, Hokkaido University, Sapporo, Japan 060-0810.
E-mail: cor@mail.sci.hokudai.ac.jp

An index of the Kuroshio Extension front strength is produced using a maximum covariance analysis between sea-surface temperature (SST) and sea-surface height (SSH) gradient observations, and composites of the atmospheric state are presented during its positive and negative phases using reanalysis data (1992–2011).

It is found that when the Kuroshio Extension is less (more) meandering, with a stronger (weaker) SST front, the atmospheric heat transport by transient eddies is increased in the western (eastern) Pacific region, consistent with an increase (decrease) in low-level baroclinicity. Analysis of the eddy–mean flow interaction shows that this zonal shift in heat transport forces anomalous barotropic flow in the Eastern Pacific, where blocking frequency is strongly influenced.

The above relationships cannot be reconciled with the known response of the North Pacific storm track to remote forcing from the Tropical Pacific, nor can they be explained by the response of the ocean to atmospheric forcing via surface heat fluxes or winds. Rather, the zonal shift in the storm track highlighted here, and the associated changes in the large-scale circulation, are interpreted as a response to the interannual variability of the Kuroshio Extension front.

1. Introduction

Subtropical western boundary currents (WBCs) transport warm water polewards which interacts with the cooler atmosphere in midlatitudes through strong air–sea heat fluxes (e.g. Kelly *et al.*, 2010; Kwon *et al.*, 2010). Hoskins and Valdes (1990) used a stationary wave model to demonstrate that such diabatic heating plays an important role in maintaining the maximum in mean baroclinicity over the midlatitude WBCs, which counteracts the tendency of growing baroclinic eddies to reduce meridional temperature gradients and the low-level baroclinicity. One mechanism by which the baroclinicity in the lower atmosphere can be maintained is by baroclinic eddies themselves, through the action of surface drag in regions of strong eddy generation (Robinson, 2000, 2006). An alternative mechanism, proposed by Nakamura *et al.* (2004), suggests that differential sensible heating across the sharp gradients in sea-surface temperature (SST) associated with WBCs enhances baroclinicity in narrow regions in the lower troposphere and effectively 'anchors' the storm track above. This hypothesis has been tested in an aquaplanet regime, with both modest enhancement of SST gradients (e.g. Inatsu *et al.*, 2003; Inatsu and Hoskins, 2004; Brayshaw *et al.*, 2008) and sharp 'frontal' SST gradients (e.g. Nakamura *et al.*, 2008; Sampe *et al.*, 2010), and with a regional atmospheric model (Taguchi *et al.*, 2009), the results indicating that the location

and structure of the storm tracks are strongly determined by the presence (or not) of regions of enhanced SST gradient in the midlatitudes, along with being highly sensitive to their latitude (e.g. Chen *et al.*, 2010; Ogawa *et al.*, 2012). Hotta and Nakamura (2011) used a stationary wave model similar to Hoskins and Valdes, with the diabatic heating decomposed into sensible and latent forcing, and found the shallow differential sensible heating in WBC regions to be crucial in maintaining near-surface baroclinicity. The sensitivity of the North Atlantic storm track to SST resolution was demonstrated in a series of high-resolution regional atmospheric model experiments by Woollings *et al.* (2010).

Given that midlatitude SST fronts may be important in determining the nature of the storm tracks, the extent to which their variability can influence the atmosphere on interannual to decadal time-scales warrants investigation. Qiu and Chen (2005) analysed sea-surface height (SSH) data over the Kuroshio Extension (KE) region and showed that the dominant variability is a bimodal interannual fluctuation between a stable state, in which the current is stronger and predominantly zonal, and an unstable state, in which the current is weaker and significantly meandering. The variability in the strength of the Kuroshio Extension Front (KEF), the strong SST front situated on the northern edge of the KE, is dominated by low-frequency fluctuations that are well correlated with the strength of the KE (Chen, 2008).

However, there are few previous studies into the storm track response to fluctuations in the KE. Joyce *et al.* (2009) found a significant but not entirely coherent relationship between the year-to-year variability of near-surface synoptic activity and small meridional shifts of the large-scale KEF (defined as the leading principle component of the 14 °C isotherm at 200 m depth). Nakamura *et al.* (2012) analysed the impact of the Kuroshio path on winter cyclone tracks over the south of Japan and showed that cyclones develop significantly faster and follow a more distinct track when the SST front is close to, rather than meandering away from, the coast. Frankignoul *et al.* (2011) investigated the large-scale atmospheric response to meridional shifts in the position of the KE using lagged regression analysis of monthly data, assuming a response time of a couple of months. The dominant signal was a weak barotropic high over the northwestern North Pacific (on the order of 0.5 hPa in sea-level pressure) lagging northward shifts in the KE by 3 months.

In this study we investigate the relationship between the Pacific storm track, large-scale atmospheric circulation, and the low-frequency fluctuations in the strength of the KEF. The data used for this study are described in section 2. An index for the KEF is derived in section 3. The observed atmospheric composites are discussed in section 4. The interpretation of ocean variability forcing the low-frequency atmospheric variability follows in section 5. Discussion of the mechanisms behind the observed relations and summarising comments are in section 6.

2. Data

To characterise the variability of the KEF we use the Advanced Microwave Scanning Radiometer–Advanced Very High Resolution Radiometer (AMSR–AVHRR) optimally interpolated daily SST dataset (Reynolds *et al.*, 2007), which is provided on a 1/4° grid from June 2002. This dataset blends available infrared and microwave satellite data. As this is a relatively short dataset, and given the correlation between KE and KEF strength (Chen, 2008), we also use the SSH satellite altimeter product from AVISO* accessed which combines measurements from the TOPEX/Poseidon, Jason and Earth Resources Satellite missions and is available daily on a 1/3° grid from October 1992 (e.g. Ducet *et al.*, 2000).

To analyse the storm track we use daily values of the temperature, T, geopotential, Φ, specific humidity, q, geopotential height, Z, and sea-level pressure (SLP), P, from the ERA-Interim reanalysis dataset (Berrisford *et al.*, 2009). We analyse the eddy heat transport, $\overline{v'h'}$, at the 850 hPa level, where v is meridional velocity and h is the moist static energy, defined as

$$h = C_p T + L_v q + \Phi. \tag{1}$$

In this expression C_p is the specific heat capacity of dry air at constant pressure and L_v is the latent heat of vaporisation, while the primes in $\overline{v'h'}$ denote high-frequency eddy variables. These are calculated using an 8-day high-pass 31-point Lanczos filter (Duchon, 1979) to effectively isolate the high-frequency synoptic-scale baroclinic eddies. The overline in $\overline{v'h'}$ refers to time mean averaging. We choose to analyse the eddy transport of moist static energy as opposed to potential temperature for example, because of its relevance for the global heat budget (e.g. Czaja and Marshall, 2006). Nonetheless, all results presented here were well reproduced by considering only the temperature field (i.e. considering $\overline{v'T'}$ rather than $\overline{v'h'}$). The large-scale atmospheric circulation anomalies are produced by removing a seasonally varying mean at each grid point, which was computed empirically at each day of the year and then smoothed using a 31-day moving average.

---

3. Kuroshio Extension Front index

To measure the covariability of the SST fronts and the KE strength, we first use the satellite data to calculate time series of the SST gradient magnitude, $|\nabla T|$, and the geostrophic surface current speed, $|\mathbf{u}_g|$, at each grid point over the upstream KE region (Figure 1(a)). To produce time series for the anomalous SST gradient and geostrophic surface current, we removed a seasonally varying mean, computed empirically at each day of the year and then smoothed using a 31-day moving average over the entire series of the respective datasets. To calculate the dominant patterns of covariability, we used a maximum covariance analysis (MCA), which involves performing a singular value decomposition on the covariance matrix of the SST gradient and velocity anomalies (e.g. Bretherton *et al.*, 1992). This operation yields patterns of variability for both fields, as well as a time series, that 'explain' decreasing amounts of covariability with increasing mode number. The squared singular values from the decomposition are proportional to the squared covariance fraction explained by each mode.

The results of the MCA between the SST gradient and current speed fields over the period of the SST time series are shown in Figure 1(a). The variability in the surface current field is a
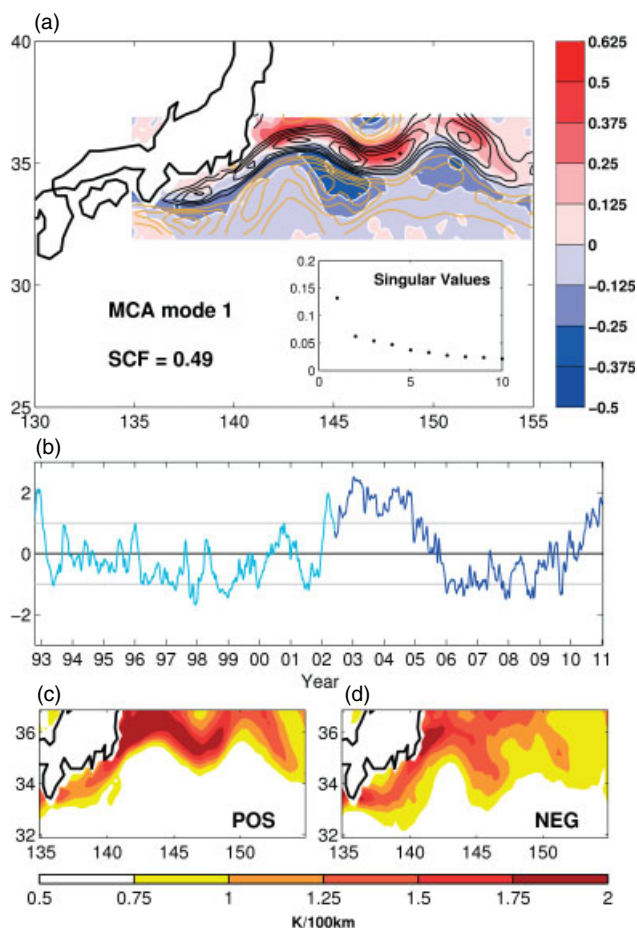

Figure 1. (a) The first mode patterns from the MCA of the surface geostrophic velocity magnitude, $|\mathbf{u}_g|(x, y, t)$, and the SST gradient magnitude, $|\nabla T|(x, y, t)$. The velocity pattern is contoured at intervals of 5 cm s^{-1} (positive in black, negative in yellow) and the SST gradient pattern is shaded in units of °C (100 km)$^{-1}$, each being equivalent to one standard deviation of the variability. Regions of negative shading are seperated by white contours. The first ten values from the singular value decomposition of the covariance matrix are plotted and the squared covariance fraction (SCF) is indicated. (b) Times series of the first mode of the MCA, normalised by one standard deviation, where the original MCA time series is in dark blue and the time series extension (computed by projecting the velocity pattern onto the full time series) is in light blue. (c) The magnitude of the SST gradient, in units of °C (100 km)$^{-1}$, corresponding the positive phase of the variability (i.e. the mean plus one standard deviation of the pattern in (a)). (d) is as (c), but for the negative phase. This figure is available in colour online at wileyonlinelibrary.com/journal/qj
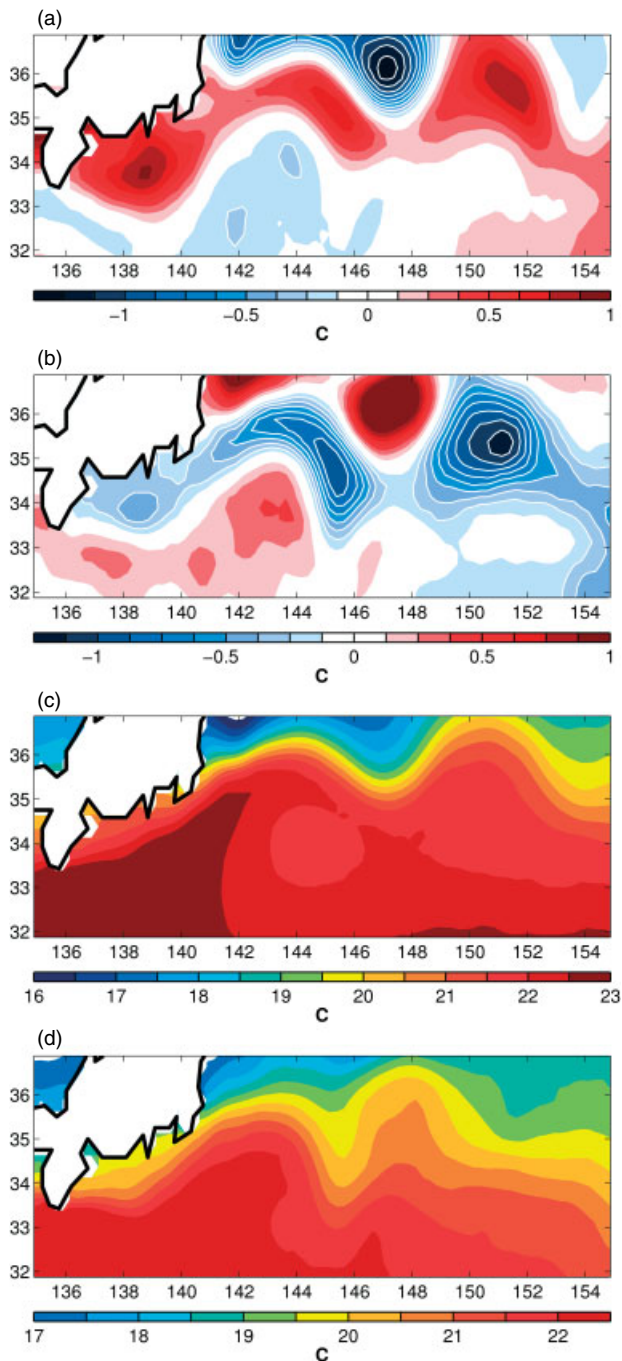
Figure 2. (a) The composite SST anomaly for the positive phase of the KEF index, $\overline{T'_{\mathrm{pos}}}$, where T' is the SST anomaly as described in the text. (b) The composite SST anomaly for the negative phase of the KEF index, $\overline{T'_{\mathrm{neg}}}$. (c) The composite SST anomaly for the positive phase of the KEF superposed on the climatological SST, $\overline{T} + \overline{T'_{\mathrm{pos}}}$, as defined in the text. (d) is as (c) but for the negative phase, $\overline{T} + \overline{T'_{\mathrm{neg}}}$. This figure is available in colour online at wileyonlinelibrary.com/journal/qj

anomaly (calculated by empirically removing the seasonal cycle as described before) in the positive and negative phases of the Kuroshio Extension index (Figure 2(a, b)), and also seen in the composite for the full (i.e. anomalies + time mean) SST field for each phase (Figure 2(c, d)). The results of the MCA analysis were found to be robust to modest changes in the region of analysis, with the strengthening/weakening of the KE being the consistent dominant feature.

To assess the thermodynamic forcing of the atmosphere by this pattern of SST variability, we produced composites of the turbulent heat flux (i.e. combined latent and sensible heat fluxes) from the ocean to the atmosphere using the Objectively Analyzed Air–Sea Fluxes (OAFlux) dataset, which is provided on a daily 1° grid (Yu *et al.*, 2008). Figure 3(a) shows the annual climatology of the turbulent heat flux (positive upwards) in the KE region. Even with the coarser resolution of the dataset, the SST gradient associated with the KEF clearly manifests itself in the turbulent heat flux field. After removing a seasonally varying seasonal cycle (calculated in the same way as for the SST), composites were produced for the positive and negative phases of the KEF index. The difference between the two phases is shown in Figure 3(b) and clearly indicates that the strengthening/weakening of the SST gradient is also captured in the heat flux field: in the positive phase of the KEF there is a strong meridional gradient in the heat flux field across the KE axis, whereas in the negative phase the gradient is reduced across the KE, which is indicative of the variable forcing of the overlying atmosphere (e.g. Tanimoto *et al.*, 2003; Taguchi *et al.*, 2012).

The time series of the first MCA mode (black line in Figure 1(b)) is dominated by interannual to decadal variability, which is similar to the variability of the KEF strength observed by Chen (2008). From the MCA analysis it is clear that the low-frequency variability is related to the state of the KE current: in the positive phase the flow is narrower and faster whilst in the negative phase it is broader and slower, corresponding to the bimodal states of the KE described by Qiu and Chen (2005).

In order to enhance statistical confidence in the subsequent analysis of the atmospheric state, we have extended the time series of this mode of SSH gradient (or geostrophic current) variability by projecting the spatial pattern of the anomalous geostrophic velocity variability (i.e. the contoured pattern in Figure 1(a)) onto the full time series of the geostrophic velocity anomaly (1992 to 2011), about ten years beyond the time duration of the blended AMSR–AVHRR dataset (section 2). The resulting time series is shown in Figure 1(b) and is used in the following to analyse the atmospheric response to variability of the KEF.

The spatial pattern of the anomalous geostrophic velocity variability that emerges from the MCA analysis closely corresponds to the first empirical orthogonal function (EOF) of the full timeseries. The spatial correlation between the patterns of the first MCA mode and the first EOF, which explain 10.1% and 11.4% of the total geostrophic velocity variance respectively, is 0.88 and the temporal correlation between the extended MCA timeseries and the principal component time series of the first EOF is 0.92. Similarly, the spatial pattern of the anomalous SST gradient magnitude of the first MCA mode and the first EOF are closely related. The spatial correlation between the patterns of the first MCA mode and the first EOF, which explain 4.3% and 4.5% of the total SST gradient variance respectively, is 0.97 and the temporal correlation between the extended MCA timeseries and the principal component timeseries of the first EOF is 0.85. On this basis, we proceed by using the extended MCA time series as an index of the dominant variability of the KEF.

4. Composite analysis of the atmospheric state

Composites of the atmospheric state on days when the KE index (i.e. the extended first MCA mode timeseries) is greater (lower) than (minus) one standard deviation from the mean (indicated by the horizontal grey lines in Figure 1(b)) were constructed
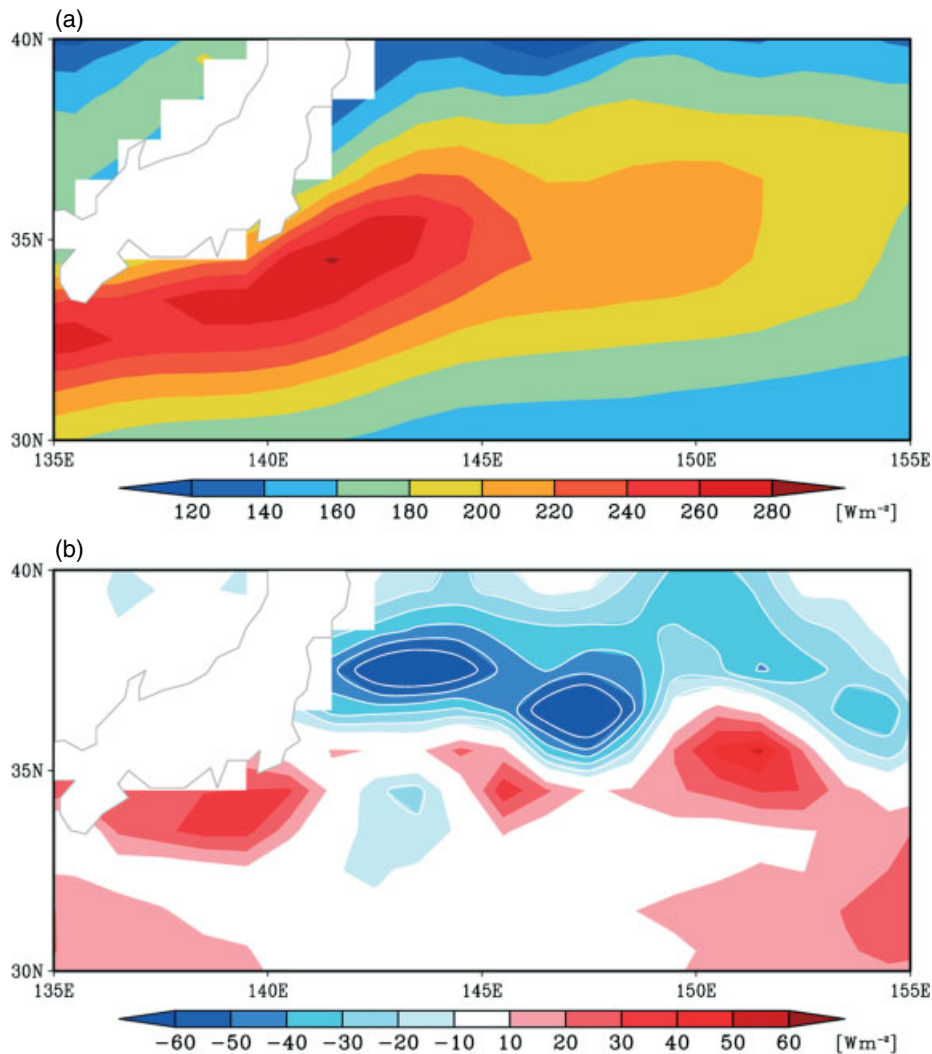
meridionally orientated dipole-like pattern (of about $20\,\mathrm{cm\,s}^{-1}$ in magnitude) and is closely matched by the pattern in the SST gradient variability (of about $0.5\,^{\circ}\mathrm{C}\,(100\,\mathrm{km})^{-1}$ in magnitude), which is slightly offset to the north of the velocity field. The singular values of the decomposition, plotted in Figure 1(a), show that the first mode is particularly dominant over the other leading modes, accounting for 49% of the squared covariance. The SST gradient fields corresponding to the positive and negative phases of the dominant mode of variability are shown in Figure 1(c) and (d) respectively. The negative anomaly of the SST gradient variability lies along the maximum gradient in the mean field and as such in the positive phase of the variability, the SST pattern exhibits a strong, sharp gradient, whereas in the negative phase the SST gradient is weaker and more diffuse. This pattern is further illustrated in Figure 2, which shows the composite SST

Figure 3. (a) The annual climatology of turbulent heat flux (the sum of latent and sensible heat fluxes, positive upwards) from the OAFlux dataset (see text). (b) The difference between the composite turbulent heat flux anomalies of the two phases of the KE index (positive minus negative). Units are W m^{-2}. This figure is available in colour online at wileyonlinelibrary.com/journal/qj

Table 1. Number of days used to produce the seasonal and annual phase composites.

Phase	Winter	Spring	Summer	Autumn	Total
Positive	325	293	272	396	1286
Negative	301	142	182	327	952

to produce maps for the positive (negative) phases of the KEF variability and the difference between the phase composites was calculated (e.g. $\overline{v'h'}_{\text{diff}} = \overline{v'h'}_{\text{pos}} - \overline{v'h'}_{\text{neg}}$). An indication of the statistical significance for the phase difference maps was computed using a Student's t-test, accounting for the persistence of the different datasets by using the effective number of degrees of freedom (e.g. Trenberth, 1984), calculated at each grid point in the respective datasets. The number of days that make up each of the phase composites for the full timeseries and for each season are shown in Table 1.

4.1. Storm track

The annual climatology of the heat transport by transient eddies, $\overline{v'h'}$, for the North Pacific over the whole period of analysis is shown in Figure 4(a). The pattern of heat transport by the transient eddies is consistent with other studies of the North Pacific storm track, with a strong maximum downstream of Japan and a southwest to northeast tilt as the storm track extends eastwards across the Pacific. This represents the lifecycle of a baroclinic

wave in which growth predominantly occurs over the western Pacific, in the vicinity of the KE, and the transient eddies develop a significant barotropic component further downstream where the heat transport is reduced (e.g. Simmons and Hoskins, 1978).

Composite plots of the eddy heat transport during the annually averaged positive and negative phases of the KEF index are shown in Figure 4(b) and (c) respectively. During the positive phase the storm track exhibits a stronger maximum over the western Pacific compared to the annual average over the full time series, whereas the heat transport is noticeably weaker over the eastern Pacific. During the negative phase of the KEF index, the heat transport maximum in the western Pacific is slightly weaker, but the region of high eddy activity extends zonally into the eastern Pacific region, where the heat transport is increased compared to the annual climatology. This zonal dependency is particularly striking in the difference between the phase composites (i.e. Figure 4(b) minus Figure 4(c)), plotted in Figure 4(d), where the storm track exhibits a zonal dipole pattern with the growing baroclinic eddies responsible for more heat transport over the western and eastern Pacific during the positive and negative phases, respectively. Figure 4(d) also indicates that there is a large degree of compensation between the two phases, such that the zonally averaged eddy heat transport over the entire Pacific storm track is essentially equal during each of the phases.

The difference in eddy heat transport between the positive and negative phases of the KEF index for each season is shown in Figure 5. The zonal dipole pattern observed in the the annual average composites is reproduced in the winter and spring but to a lesser extent in the autumn. The composite in the summer is
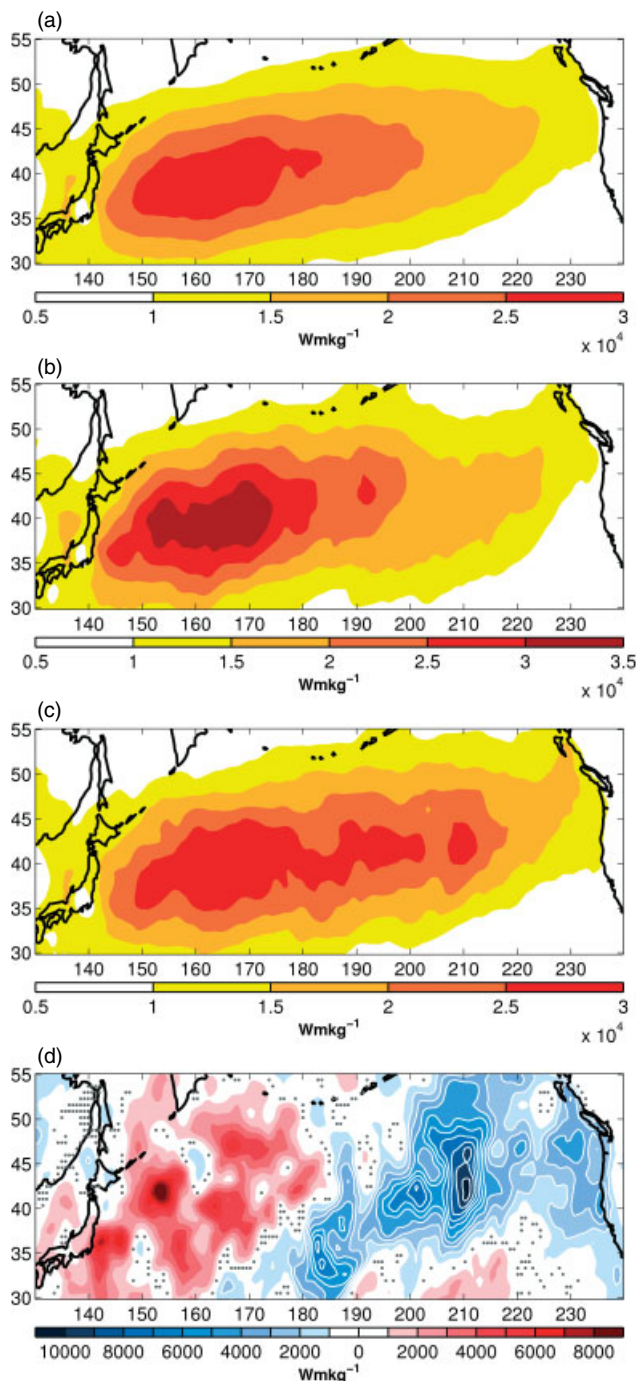
Figure 4. The annual averages for (a) the eddy heat transport climatology for the full time series, $\overline{v'h'}_{\text{full}}$, (b) the eddy heat transport for the positive phase of the KEF index, $\overline{v'h'}_{\text{pos}}$, and (c) the eddy heat transport for the negative phase of the KEF index, $\overline{v'h'}_{\text{neg}}$. (d) shows the difference between the annually averaged eddy heat transport in the positive and negative phases of the KEF index, $\overline{v'h'}_{\text{diff}}$, and the stippling indicates regions where the statistical significance is less than 90%. This figure is available in colour online at wileyonlinelibrary.com/journal/qj

very weak and there is no obvious dipole signal, which we may expect since the storm track is significantly weaker and situated to the north of the KE in the summer. The seasonal analysis thus reveals that it is primarily winter and spring that contribute to the zonal dipole pattern in the Pacific storm track.

4.2. Large-scale circulation

Composites of SLP and geopotential height anomalies at the 500 hPa level are now considered. The annual average composites for the SLP anomalies in the positive and negative phases are shaded in Figure 6(a) and (b) respectively, with the associated 500 hPa geopotential height anomaly composites superimposed
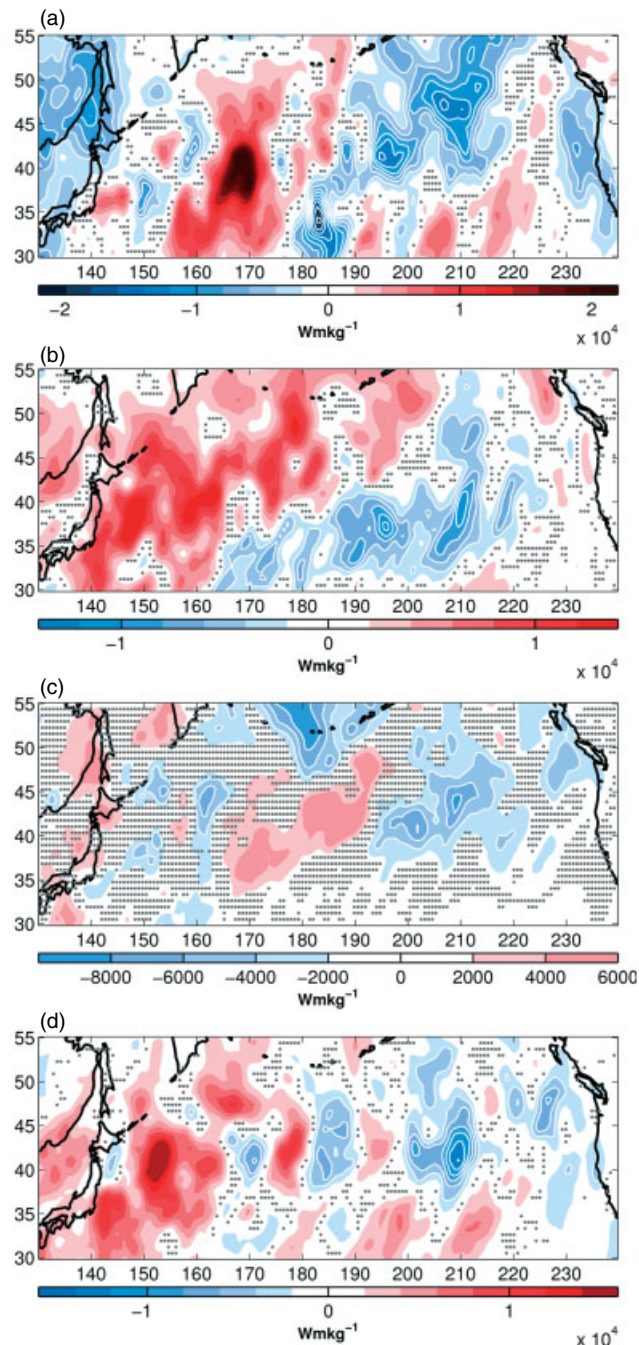

Figure 5. The difference between the eddy heat transport in the positive and negative phases of the KEF index, $\overline{v'h'}_{\text{diff}}$ for: (a) winter (i.e. DJF), (b) spring (i.e. MAM), (c) summer (i.e. JJA), and (d) autumn (i.e. SON). The stippling indicates regions where the significance is less than 90%. This figure is available in colour online at wileyonlinelibrary.com/journal/qj

in contours. The positive composite map, Figure 6(a), indicates an equivalent barotropic high pressure anomaly over the east Pacific, in the vicinity of Alaska, located to the north of a weaker equivalent barotropic low pressure anomaly. In the western Pacific there is a weaker meridional dipole, with a weaker barotropic component, of opposite sign creating an anomalous quadrupole pattern in the Pacific SLP field during the positive phase. The equivalent plot for the negative phase of the KEF index is shown in Figure 6(b), where an equivalent barotropic meridional dipole structure, of opposite sign to that of the positive phase, is observed in the eastern Pacific. In the western Pacific region there is no corresponding opposite dipole structure. The composite phase difference, shown in Figure 6(c), emphasises the opposite circulation response. The difference plot shows an equivalent barotropic meridional dipole structure in the eastern Pacific region, whereas no clear structure emerges in the western Pacific region in the vicinity of the KE. In relation to the mean flow, this represents a
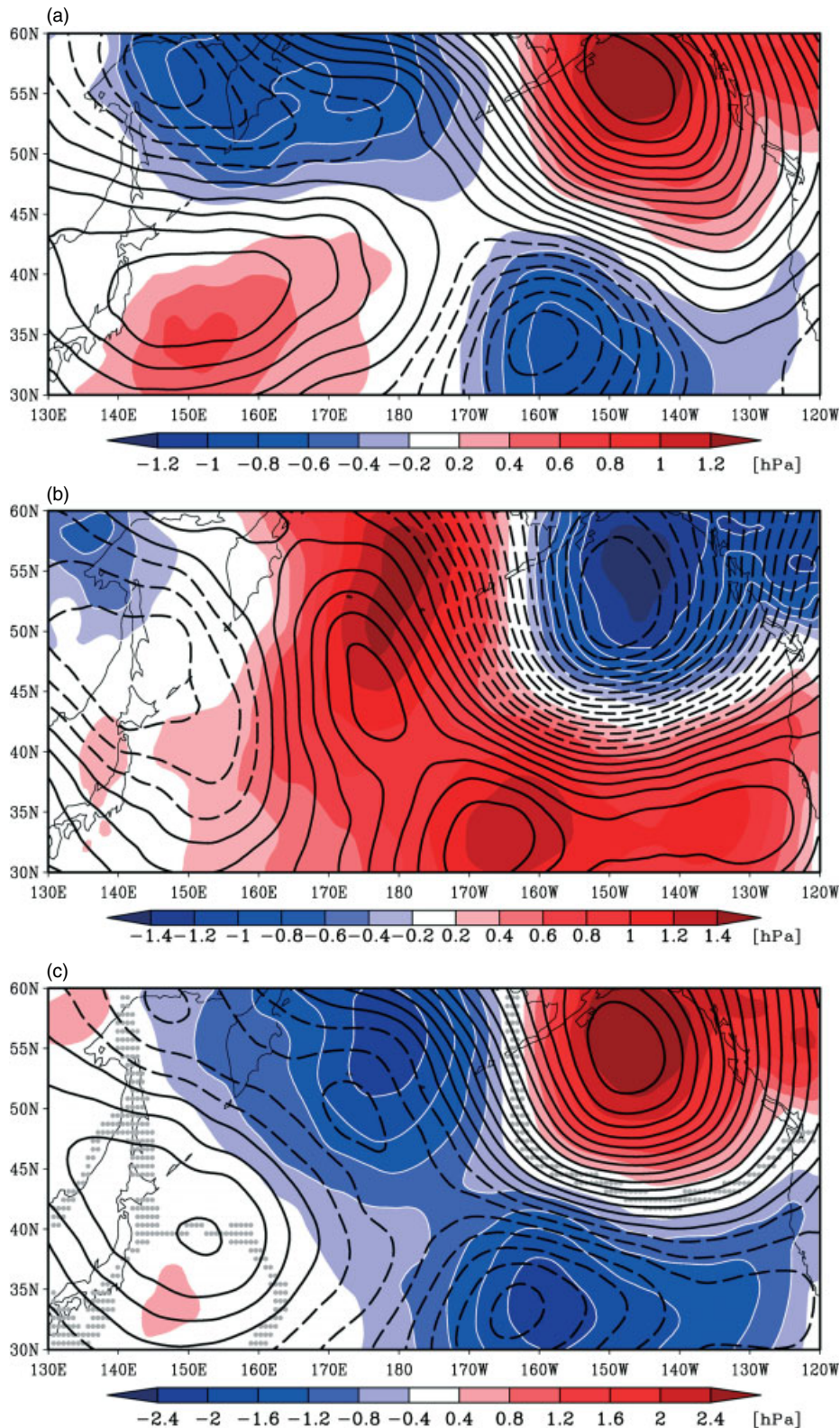
Figure 6. (a) Annual average sea-level pressure anomaly (hPa, shading) for the positive phase of the KEF index, $\overline{P'_{pos}}$, where P' is the sea-level pressure anomaly as described in the text (stippling indicates regions where the statistical significance is less than 90%). Overlayed are contours showing the annual average 500 hPa geopotential height anomaly during the positive phase of the KEF index, $\overline{Z'_{pos}}$, with a contour interval of 2 m (i.e. . . . , $-5, -3, -1, 1, 3, 5, . . .$) where positive contours are solid and negative contours are dashed. (b) is as (a) but for the negative phase of the KEF index. (c) shows the difference between the two composites, $\overline{P'_{diff}}$, where the stippling indicates that the significance is below 90%. Here $\overline{Z'_{diff}}$ is contoured with an interval of 4 m (i.e. . . . , $-10, -6, -2, 2, 6, 10, . . .$). This figure is available in colour online at wileyonlinelibrary.com/journal/qj

weakening of the barotropic flow in the eastern Pacific during the positive phase of the KEF index and a strengthening in the negative phase.

The composite differences of the large-scale circulation for each season are shown in Figure 7. In the winter, the meridional equivalent barotropic dipole signal from the annual average is evident in the eastern Pacific region albeit centred slightly further

north. The dipolar structure is also clear in the spring, centred to the south of the winter dipole response. The composite in the autumn is weaker and somewhat noisier than the winter and spring with no obvious meridional barotropic dipole over the eastern Pacific. Similarly, the summer composite is weak and noisy and does not resemble the pattern seen in the annual average. It is notable that the smaller horizontal scale of the
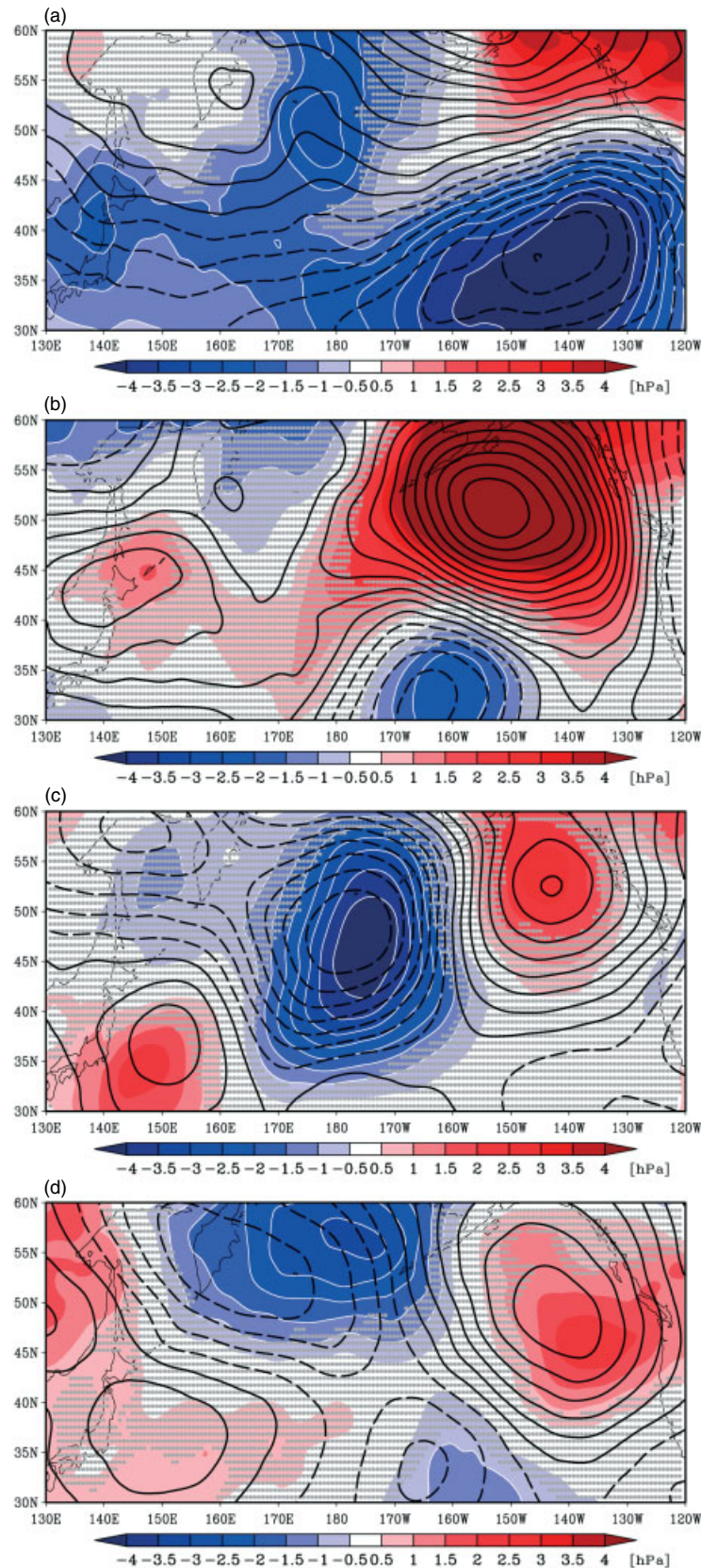
Figure 7. The difference (hPa, shading) between the two seasonal composites $\overline{P'_{\mathrm{diff}}}$ (where stippling indicates that the significance is below 90%) for: (a) winter (i.e. DJF), (b) spring (i.e. MAM), (c) summer (i.e. JJA), (d) autumn (i.e. SON). $\overline{Z'_{\mathrm{diff}}}$ is contoured with an interval of 8 m (i.e. . . . , $-20, -12, -4, 4, 12, 20, . . .$). This figure is available in colour online at wileyonlinelibrary.com/journal/qj

geopotential height anomalies in the summer is consistent with stationary Rossby waves, whose wavelength is proportional to the square root of the mean westerly wind speed. The seasonal difference plots reveal that it is the winter and spring that strongly determine the meridional equivalent barotropic dipole in the large-scale circulation anomaly over the eastern Pacific region seen in the annual mean.

4.3. Eddy–mean flow forcing

We now consider whether the weakening and strengthening of the zonal barotropic flow in the eastern Pacific is a consistent manifestation of the storm track zonal dipole forcing on the mean flow. Hoskins *et al.* (1983) demonstrated that the feedback of transient eddies on the barotropic time-mean flow can be

measured through the vector

$$\mathbf{E} = (E_x, E_y) = (\overline{v'^2 - u'^2}, -\overline{u'v'}),$$

where the primes denote high-pass-filtered eddy components and the overbar denotes time averaging. The horizontal components of the $\mathbf{E}$ vector are measures of the eddy anisotropy, where the zonal component, E_x, is a measure of the eddy shape (i.e. points westwards for zonally elongated eddies and eastwards for meridionally elongated eddies), and the meridional component, E_y, is a measure of orientation, and the divergence of the $\mathbf{E}$ vector acts to accelerate the zonal mean flow.

We choose to narrow our investigation to the winter and spring in the light of the strong zonal dipole in the storm track during these seasons. The raw maps of $\nabla \cdot \mathbf{E}$ are dominated by small-scale structure so, to ascertain the feedback on the large-scale circulation, the maps presented here have been smoothed by plotting a $10° \times 10°$ spatial average at each grid point. Figure 8(a) shows a plot of the climatology of $\nabla \cdot \mathbf{E}$ at the 300 hPa level during the winter and spring (i.e. DJFMAM) over the full duration of the time series. As in previous studies, the meridional elongation of barotropic eddies in the entrance and middle of the Pacific storm track, due to growing baroclinic waves, is found to generate a divergence of the $\mathbf{E}$ vector and an acceleration of the barotropic westerly flow that peaks over the midlatitude central Pacific, whereas in the storm-track exit region and on the meridional flanks of the storm track there is convergence of the $\mathbf{E}$ vector, indicating a tendency for the eddies to decelerate the westerly flow in these regions.

Figure 8(b) is a composite map of the $\mathbf{E}$ vector divergence during the positive phase of the KEF index. The $\mathbf{E}$ vector divergence appears slightly larger over the western Pacific region, with a maximum divergence over the centre of the storm track that is located slightly further upstream than in the mean (i.e. Figure 8(a)). The region of $\mathbf{E}$ vector divergence does not extend as far into the eastern Pacific region as in the mean. These observations are a reflection of the zonal localisation of the storm track in the western Pacific during the positive phase of the KEF index, when the SST gradient of the KEF front is stronger. The $\mathbf{E}$ vector divergence during the negative phase of the KEF, shown in Figure 8(c), is diminished over the western Pacific region and instead is strongest over the eastern Pacific region, indicative of increased barotropic westerlies in this region.

The difference between the two phases is shown in Figure 8(d). The increased $\mathbf{E}$ vector divergence between 40°N and 50°N over the eastern Pacific region during the *negative* phase of the KEF index is evidently a reflection of the storm-track dipole that emerged from analysis of the eddy heat transport. When the eddy heat transport is predominantly over the western Pacific, during the positive phase of the KEF index, the meridional elongation of the barotropic eddies occurs primarily over the entrance and middle of the storm track. However, in the negative phase of the KEF index, baroclinic wave growth increases over the eastern Pacific and, as a result, the $\mathbf{E}$ vector divergence is found to increase there. The observed transient eddy forcing of the large-scale barotropic westerly flow over the eastern Pacific region is therefore consistent with the observed decrease and increase of the barotropic flow during the respective positive and negative phases of the KEF index.

4.4. North Pacific blocking

The enhanced storm track in the western North Pacific during the positive phase of the KEF is reminiscent of the behaviour preceding the onset of an Alaskan blocking event in the eastern North Pacific, as observed by Nakamura and Wallace (1990). Their study supported the idea, first proposed by Green (1977), that baroclinic wave activity is important in maintaining anticyclonic blocking anomalies. The map of the SLP and 500 hPa geopotential height anomaly found in the positive phase of the

KEF, in Figure 6(a), shows a familiar barotropic blocking pattern with a high pressure anomaly to the north of a low pressure anomaly, suggestive of an increase in the prevalence of blocking flows when the KEF is in the positive phase, whilst the opposite flow pattern in the negative phase is indicative of less blocking.

To test this hypothesis, we computed a blocking index over the North Pacific over the period of the KEF index, again using the ERA-Interim reanalysis dataset. Following the method of Barriopedro et al. (2006), we produced an adapted version of the Tibaldi and Molteni (1990) index. Two geopotential height gradients (GHGN and GHGS) are calculated at each longitude for each day of the KEF index:

$$\mathrm{GHGN} = \frac{Z(\lambda, \phi_N) - Z(\lambda, \phi_0)}{\phi_N - \phi_0}, \quad (2)$$

$$\mathrm{GHGS} = \frac{Z(\lambda, \phi_0) - Z(\lambda, \phi_S)}{\phi_0 - \phi_S}, \quad (3)$$

for $\phi_N = 77.5°N + \Delta$, $\phi_0 = 60.0°N + \Delta$, $\phi_S = 40.0°N + \Delta$; $\Delta = -5.25°, -3.0°, 0.0°, +3.0°, +5.25°$. Here $Z(\lambda, \phi)$ is the 500 hPa geopotential height at longitude λ and latitude ϕ. At a particular longitude a blocking flow configuration is identified when GHGN and GHGS satisfy the following conditions for at least one of the five values of Δ:

$$\mathrm{GHGN} < -10 \, \mathrm{gpm \, deg}^{-1}, \qquad \mathrm{GHGS} > 0, \quad (4)$$

along with the condition that the geopotential height anomaly at ϕ_0 must be positive. The blocking index was then refined to include only blocking features that spanned at least 13.5° in longitude (allowing for one non-blocking longitude between two blocking longitudes) and were at least 5 days in duration (allowing for one non-blocking day between two blocking days).

The climatology of the blocking frequency for the combined spring and winter (i.e DJFMAM), in days per 6 months, over the full series of the KEF index is plotted in Figure 9(a). We again choose to focus on the spring and winter months, when the zonal storm track dipole is most apparent. We also produced composite blocking indices for the positive and negative phases of the index and the difference between the two is plotted in Figure 9(b). Regions where the difference between the two blocking indices is significant at the 90% level was determined using Student's t-test, as before, accounting for persistence to calculate the effective number of degrees of freedom. Figure 8(b) indicates that, during the positive phase of the KEF index, when the KE is associated with a strong SST front, there is significantly more blocking over the Alaskan region of the eastern North Pacific.

Hoskins et al. (1983) and Shutts (1986) explicitly demonstrated that during the period of a blocking event there is $\mathbf{E}$ vector convergence across the region of the easterly blocking flow. As such, the difference in blocking frequency between the two phases, in Figure 9(b) is consistent with the eddy–mean flow analysis in section 4.3. The increase in the blocking frequency (and hence periods of $\mathbf{E}$ vector convergence) in the positive phase of the KEF compared to the negative phase is reflected in the observed reduction in $\mathbf{E}$ vector divergence in the positive phase compared to the negative phase over the eastern North Pacific (i.e. Figure 8).

5. Interpretation as an atmospheric response to Kuroshio Extension variability

The analysis presented above implies correlation between the state of the KE and the state of the atmosphere but it does not necessarily imply causality. In one line of thought, one might interpret the covariability between KE and atmospheric variables to be driven remotely from the Tropical Pacific in view of large variability exhibited by the Pacific basin on interannual and decadal time-scales (e.g. Zhang et al., 1997). Alternatively, one might interpret
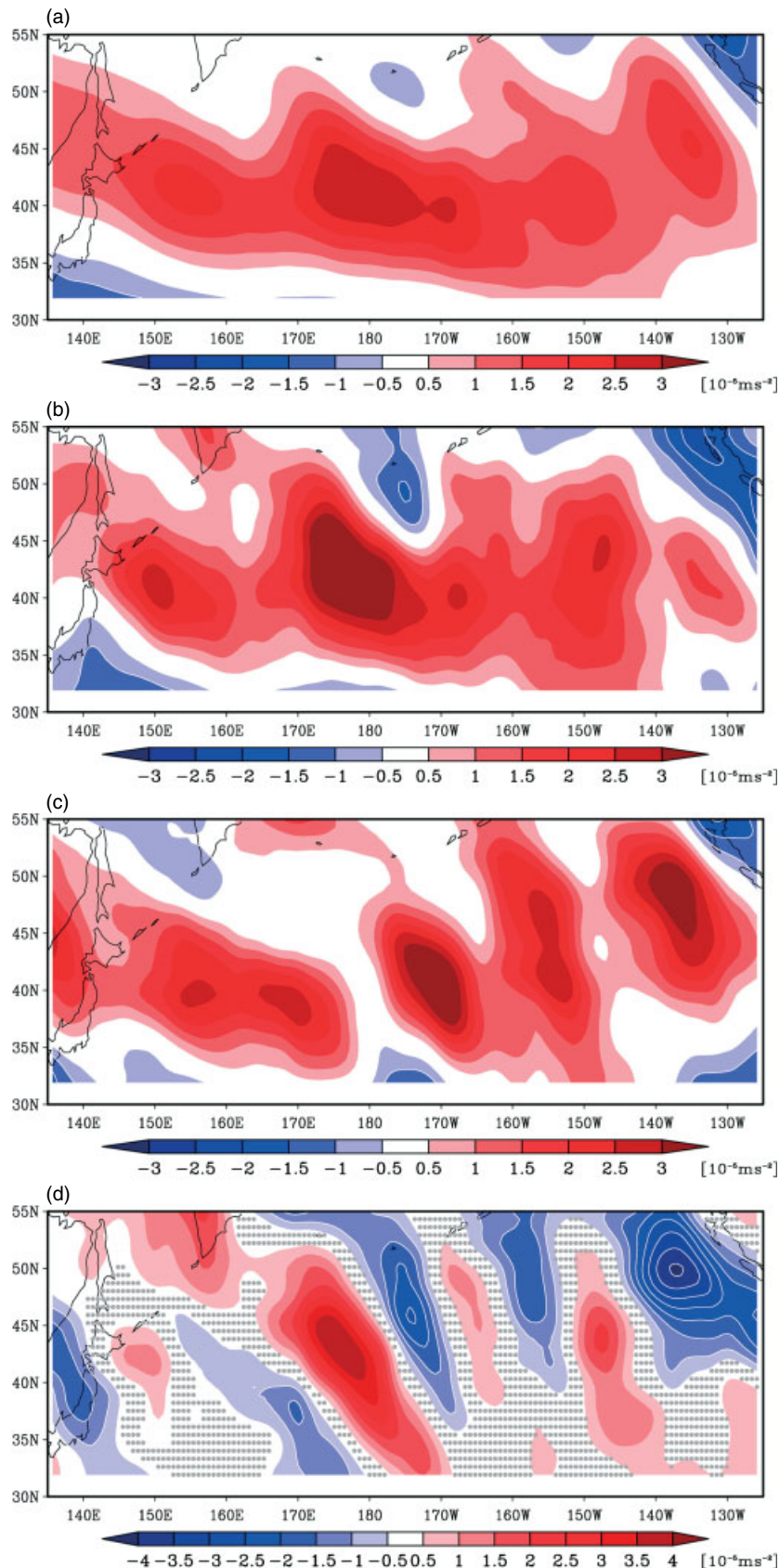
Figure 8. (a) The climatological $\nabla \cdot \mathbf{E}$ calculated at 300 hPa for boreal winter and spring (the data have been smoothed using a $10° \times 10°$ spatial average calculated at each point as described in the text). (b) is as (a) but for the positive phase of the KEF index. (c) is as (a) but for the negative phase of the KEF index. (d) shows the difference between the positive and negative composites. Regions in which the statistical significance is less than 90% are indicated by stippling. This figure is available in colour online at wileyonlinelibrary.com/journal/qj

the results in section 4 as reflecting intrinsic ocean–atmosphere interactions over the North Pacific –either atmospheric forcing of the ocean, oceanic forcing of the atmosphere, or both. In this section, we discuss in turn these views and suggest that oceanic forcing of the atmosphere is key to explaining the relationships outlined in section 4.

To analyse Tropical Pacific forcing, we produced SST composite maps for the positive and negative phases of the KEF index over the Tropical Pacific using the NOAA $1° \times 1°$ optimally interpolated weekly SST dataset (Reynolds and Smith, 1994) for the entire length of the KEF index (which was weekly averaged to match the temporal resolution of the SST product).
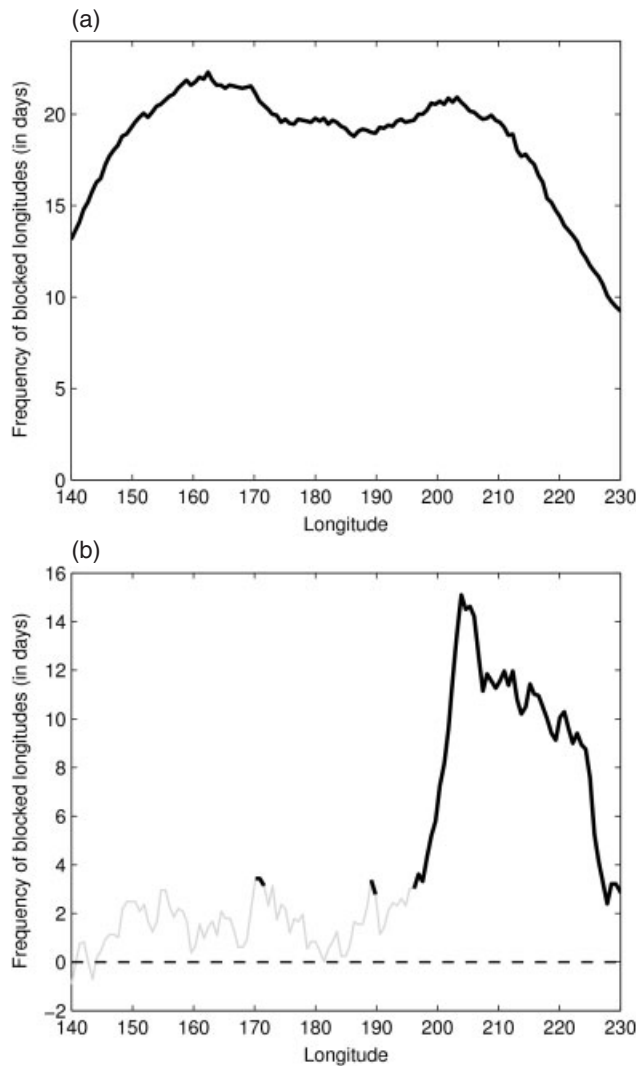
Figure 9. (a) Climatology of blocking frequency (calculated using the blocking index described in the text) for the boreal winter and spring (i.e. DJFMAM) over the period of the KEF index, in number of days per 6 months. (b) The difference between the composite blocking indices for the positive and negative phases of the KEF index, plotted in bold where the difference exceeds 90% significance.

The SST anomaly during the positive phase of the KEF index (shown in Figure 10(a)) for the winter and spring months (i.e. DJFMAM), when the zonal dipole in heat transport anomalies was detected in section 4, consists of a broad positive anomaly over the central equatorial Pacific that peaks at about $+0.3°$ K and a narrower region of negative SST anomaly in the eastern equatorial Pacific that reaches about $-0.3°$ K. The composite SST anomaly during the negative phase of the KEF index in the winter and spring, shown in Figure 10(b), consists of a narrow negative anomaly over the central equatorial Pacific that peaks at about $-0.3°$ K, with no other clear features. The difference between the composites is plotted in Figure 10(c) along with an indication of the statistical significance of the temperature difference, calculated using Student's t-test, where the stippling indicates where the significance level is less than 90%. As can be seen, almost all of the equatorial SST anomalies are stippled, indicating a lack of statistical significance. This is due to a combination of the strong persistence of SST anomalies in this region, which reduces the effective number of degrees of freedom during the period of the KEF index, and the large standard deviation of SST associated with the El Niño–Southern Oscillation (ENSO), which is greater than $1°$ K across most of the equatorial Pacific region (e.g. Deser *et al.*, 2010).

A more meaningful indication that the statistical relationships presented in section 4 are not dominated by a clear ENSO signal perhaps comes from comparison with previous studies of the the atmospheric response to ENSO. The dominant stationary

wave pattern that is observed in response to the warm phase of ENSO in the North Pacific consists of an anomalous anticyclone over the Pacific at lower latitudes and anomalous cyclonic flow in the northern region of the Pacific (Horel and Wallace, 1981; Trenberth *et al.*, 1998). This differs from the composite large-scale circulation response during the positive phase of the KEF index, which exhibits a high anomaly over the northeastern Pacific, during which there is a broad warm anomaly in the central equatorial Pacific. The large-scale circulation anomalies that emerge in our KEF index composite, with a warm/cold anomaly in the equatorial Pacific, are essentially in the opposite sense to the observed circulation response to ENSO.

The same can be said for storm track changes. During El Niño, the Pacific storm track is displaced southwards and strengthens further downstream over the eastern Pacific, likely in response to the enhanced large-scale baroclinicity on the poleward edge of the tropical Pacific that arises due to tropical warming (Hoerling and Ting, 1994; Trenberth and Hurrell, 1994; Orlanski, 2005; Seager *et al.*, 2005). In the negative phase of our KEF index, when the storm track is seen to extend eastwards, Figure 9(b) indicates the presence of a weak cold anomaly in the equatorial Pacific. During the positive phase of the KEF index, during which there is a warm anomaly in the equatorial Pacific (i.e. Figure 9(a)), the storm track is seen to be primarily localised over the western North Pacific. Thus the storm track changes in the composite analysis above do not resemble an atmospheric response to an equatorial SST anomaly.

Finally, studies of blocking frequency over the northeastern Pacific reveal that during the warm phase of ENSO the number of blocked days decreases, whereas the blocking frequency increases during the cool phase of ENSO (Renwick and Wallace, 1996; Compo *et al.*, 2001; Carrera *et al.*, 2004). Here we observe a warm tropical SST anomaly during the positive phase of our KEF index (i.e. Figure 9(a)), when we find increased blocking frequency over the northeastern Pacific, i.e. opposite to the observed behaviour during El Niño periods. The opposite occurs during the negative phase of the KEF index, where we observe a cool equatorial SST anomaly and a decrease in blocking frequency.

The previous discussion makes it clear that the statistical relationships established in section 4 are unlikely to result from tropical forcing. Let us now turn our attention to extratropical ocean–atmosphere interactions, starting with the response of the ocean to local atmospheric forcing. Inspection of the composite difference for SLP between positive and negative phases of the KEF index (Figure 6(c)) shows no significant anomalies over the region where the SST gradients are perturbed (Figure 1(a), shaded). From geostrophy, this indicates no significant changes in surface winds and, as a result, it rules out a local forcing via anomalous Ekman currents, or wind-induced changes in surface heat fluxes. Indeed, Figure 3 supports the view that surface heat fluxes actually damp the SST anomaly associated with the KEF index. We thus rule out a local atmospheric forcing and focus on geostrophic advection as the main driver of the SST anomaly associated with the KEF index.

It is well established from a vast body of literature that changes in strength and location of the KEF reflect wind-driven forcing, with positive values (northward shift and intensification) being driven, with a time lag of a few years, by anticyclonic wind-stress curl in the central and eastern Pacific (e.g. Qiu and Chen, 2005; Sasaki *et al.*, 2013). However the wind-stress curl composites associated with our KEF index at zero lag shows cyclonic wind-stress curl over the central and eastern Pacific (Figure 11(b), red colours), with a Sverdrup response tending to weaken the Kuroshio (Figure 11(b, c)). This is very interesting because the composite of atmospheric circulation changes at zero lag (e.g. Figure 6(c)) is significant: thus there must be a physical mechanism linking the anticyclonic wind stress causing the shift and intensification of the KEF to the subsequent cyclonic wind stress found a few years later once the KEF has shifted and intensified. Following the analysis of such oscillatory behaviour
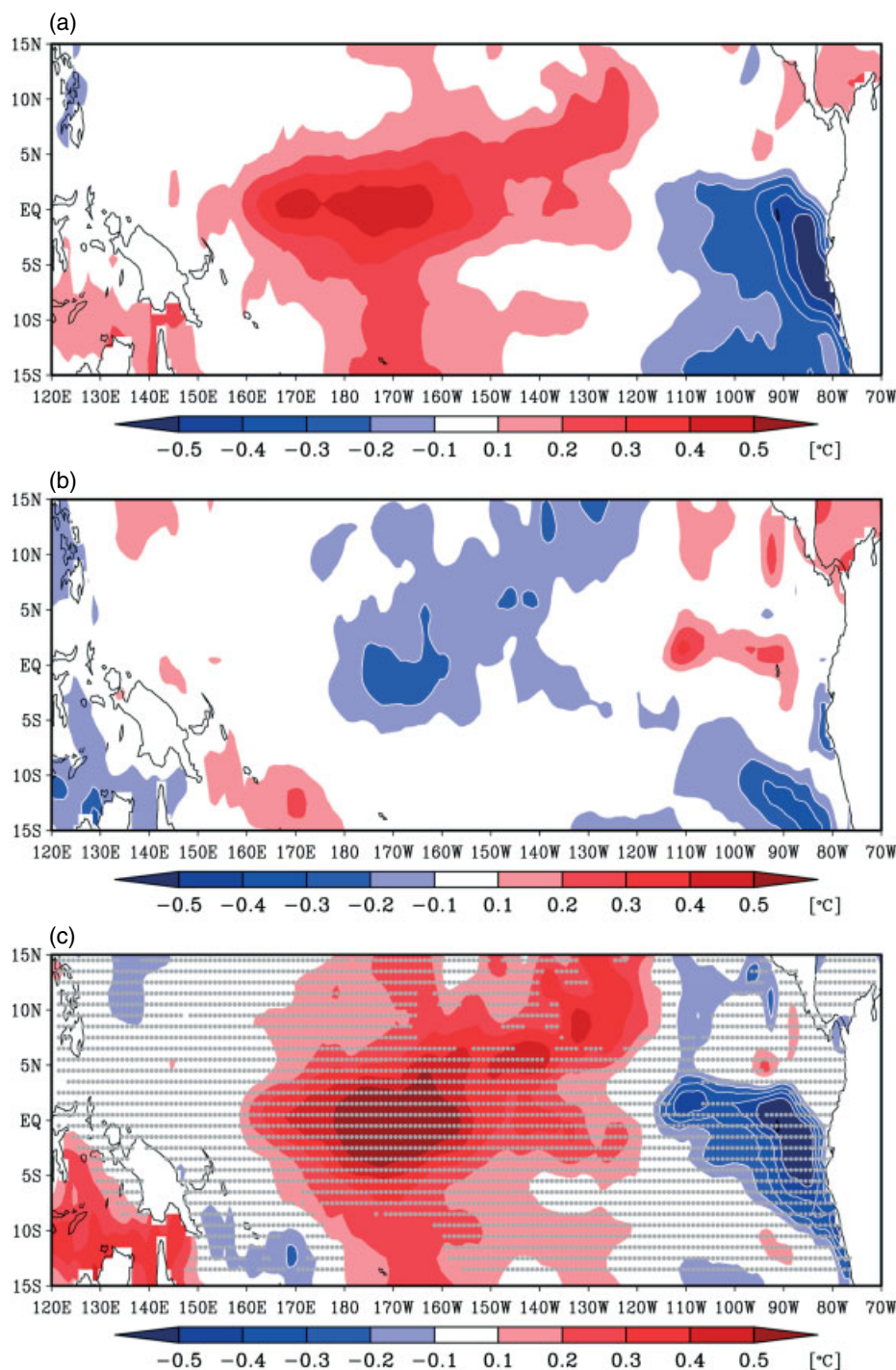
Figure 10. (a) The composite SST anomaly in the tropical Pacific for the positive phase of the KEF index. (b) is as (a) but for the negative phase of the KEF index. (c) shows the difference between the phase composites, and the stippling indicates regions in which the statistical significance is less than 90%. This figure is available in colour online at wileyonlinelibrary.com/journal/qj

by Qiu *et al.* (2007), we suggest that the physical mechanism, and thereby the interpretation of the composites in section 4, is an oceanic feedback in which a stronger and poleward-shifted KEF destabilises the atmosphere more strongly over the Western Pacific, leading to intensified poleward heat transport and, through the eddy–mean flow interactions shown in section 4.3, to the anomalous circulation depicted in Figure 6(c).

6. Summary and discussion

In this study we have investigated the covariability of the KEF and the North Pacific storm track. We produced an index of the KEF spanning 19 years using satellite observations of SST and SSH. In the positive phase of the index, the SST gradient across the KE is strong, whereas in the negative phase the KE meanders more and the KEF is relatively weak. A similar pattern is also seen in maps

of the turbulent heat flux, albeit at a coarser resolution, indicating that this SST varability results in a variation of the forcing on the overlying atmosphere. This index was used to produce composites of the atmospheric state in its positive and negative phases. After consideration of the response of the geostrophic ocean circulation to wind changes, and consideration of the response of the North Pacific atmospheric circulation to ENSO variability, it was concluded that the composite atmospheric states in the positive and negative phases of the KEF index can be taken as proxies for the response of the North Pacific storm track to weakening/strengthening of the SST gradient along the KE.

The observed storm track response is consistent with the enhancement of low-level baroclinicity across a sharp SST front, confirming what has been previously highlighted in modelling studies. When the KE is in a stable state characterised by a narrower and stronger current, the SST gradient across the KEF is stronger
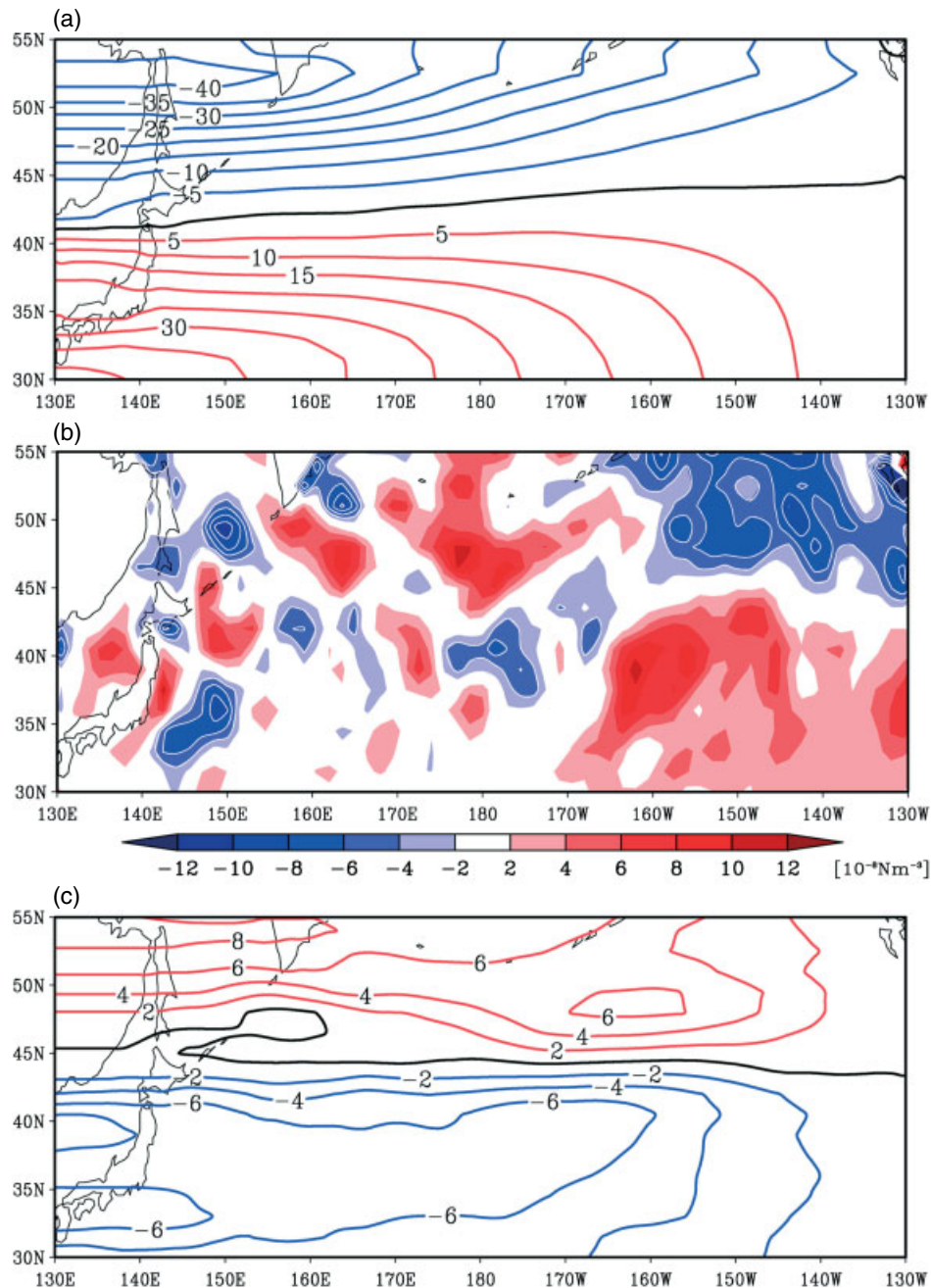
Figure 11. The annual averages for (a) the depth-integrated geostrophic streamfunction for the full dataset, $\overline{\Psi_0}$, and (b) the wind-stress curl difference between the positive and negative phases of the Kuroshio Extension front, $\nabla \times \overline{\tau_{\text{diff}}}$. (c) shows the difference in depth-integrated geostrophic streamfunction between the positive and negative phase, $\overline{\Psi_{\text{diff}}}$, calculated from the wind-stress curl difference in (b). The streamfunction is plotted over the continents but it has obviously no meaning there. This figure is available in colour online at wileyonlinelibrary.com/journal/qj

and eddy heat transport is found to be zonally localised in the western Pacific region, with less heat transport by growing eddies downstream in the eastern Pacific region. Our interpretation is that, in the presence of the strong surface temperature gradient, the baroclinic waves grow faster and quickly become significantly barotropic and, as such, are not advected very far downstream during their growth phase. As a result, there is more heat transport by transient baroclinic eddies in the western Pacific during the positive phase of the KEF. On the other hand, when the KEF is the negative phase, the growth rate of the baroclinic eddies in the presence of a weaker surface temperature gradient is slower, and the latter are advected further downstream by the background westerly flow into the eastern Pacific, where an increased eddy heat transport is observed.

Two further points are worth mentioning relating to the mechanisms through which the KEF can impact surface baroclinicity. Firstly, it should be noted that, whilst the SST front appears to influence the low-level baroclinicity, it is the background subtropical jet that is main source of available

potential energy upon which the eddies feed, and that ultimately determines the strength of the whole storm track. This is indicated by the compensation in the storm track dipole between the heat transport in the western and eastern Pacific (i.e. Figure 3(d)). The fluctuation of the SST front is interpreted as a perturbation to the mean state, zonally localising the storm track more effectively over the western Pacific when the surface SST gradient is strong and having less influence on the overlying atmosphere when the SST front is weaker. This influence of surface temperature gradients on growth rate is consistent with cyclogenesis from a potential vorticity (PV) perspective (Hoskins *et al.*, 1985). Second, it is not explicitly clear at this stage exactly how the changes in SST highlighted here lead to changes in eddy heat transport. The composite in SLP and geopotential height at 500 hPa in Figure 5(c) displays a weak reduction in the vertical zonal wind shear north of 35°N, where, in contrast, comparison of Figure 1(c, d) shows a strengthening of the SST gradient. Thus, the latter does not seem to penetrate over the lower atmosphere (if it did, thermal wind arguments would imply a strengthening of the westerly
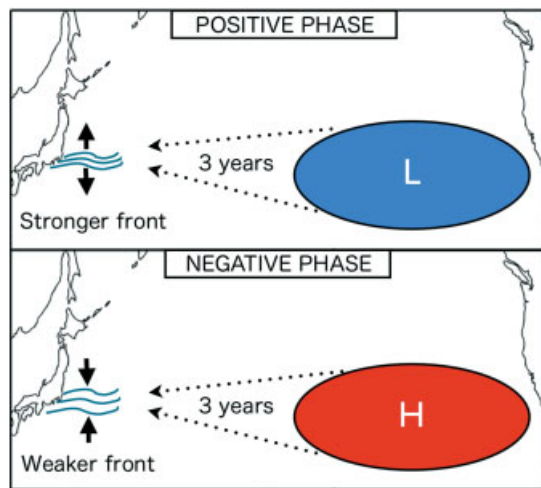
Figure 12. Schematic of the potential mode of coupled ocean–atmosphere variability as discussed in the text. This figure is available in colour online at wileyonlinelibrary.com/journal/qj

wind shear between the surface and 500 hPa) and the greater instability might instead reflect changes in stratification. Indeed, we emphasise that, in the positive phase of our KEF index, SSTs are also higher south of the KEF, and convective processes may thus play a role in maintaining a low Richardson number over the KE (Sheldon and Czaja, 2014). More work is needed to clarify this issue.

The response of the annually averaged large-scale atmospheric circulation to the KEF is a meridionally orientated dipole anomaly in the eastern Pacific, with a reduction of the barotropic westerlies flows when the KEF is stronger and an enhancement when the KEF is weaker. Seasonal analysis reveals that the response to the KEF index by both the storm tracks and the large-scale circulation is strongest in the winter and spring. We analysed the eddy–mean flow forcing and found that the anomalous large-scale barotropic flow over the eastern Pacific is consistent with the low-frequency variability of transient eddy forcing. When the storm track is stronger in the western Pacific, during the positive phase of the KEF, the eddy-driven barotropic flow in the eastern Pacific is reduced, whereas when the storm track is stronger in the eastern Pacific, during the negative phase of the KEF, the eddy-driven barotropic flow in the eastern Pacific is increased.

The impact of the KEF index on the frequency of blocking patterns over the northeastern Pacific was analysed by computing a simple blocking index. During the winter and spring seasons, the frequency of blocking is found to increase substantially over the northeastern Pacific region during the positive phase of the KEF index. This is consistent with the reduced **E** vector divergence over the same region during the positive phase compared to the negative phase. An interpretation of this in terms of the barotropic eddy-straining blocking mechanism of Shutts (1983) is outlined in the Appendix.

The large-scale flow driven observed in the eastern Pacific suggests that there is the potential for a coupled ocean–atmosphere decadal oscillation over the North Pacific. The study by Sasaki *et al.* (2013) shows that the broad positive SSH anomalies in the eastern Pacific, driven by an anomalous anticyclonic wind field across the latitudes of the KE region, generate a strengthening of the KE three years later. However, we have shown that, when the KE jet is strong, this drives a large-scale cyclonic anomaly in the eastern Pacific, which the observational study by Sasaki *et al.*, suggests will act to weaken the KE approximately three or so years later. From our study, we expect the weaker KE to drive a large-scale anticyclonic anomaly in the eastern Pacific and so on (the schematic in Figure 12). Coupled decadal modes of variability have been studied in coupled general circulation models (e.g. Kwon and Deser, 2007) and in an observationally constrained study using an idealised model by Qiu *et al.* (2007), although

these studies have focussed on the impact of broader-scale SST anomalies in the KE region rather than the variability of the KEF itself. Key to these type of studies is the existence of an impact of the SST anomalies in the KE region on the large-scale atmospheric circulation. With respect to this issue, the quadrupolar pressure signal attributed here to a northward shift and intensification of the KEF (i.e. Figure 5(a)) is different from that inferred by Frankignoul *et al.* (2011) in the NCEP–NCAR[†] reanalyses – these authors isolated a dipolar structure over the northwestern Pacific. We note however that the SST pattern considered in Frankignoul *et al.* (2011) is very different from ours, showing a uniform warming across the KEF (their Figure 6, bottom panel) rather than a dipolar structure (our Figure 2).

The fact that the storm track exhibits a large-scale response to variability in strength of the KEF highlights the importance of WBCs in determining the dynamics of the midlatitude troposphere. In particular, this study suggests that understanding the low-frequency variability and potential predictability of the KE could have particular importance in understanding the observed low-frequency variability in storm tracks (e.g. Chang and Fu, 2002; Nakamura *et al.*, 2002), decadal variability of blocking flows over the eastern Pacific (e.g. Chen and Yoon, 2002) and associated periods of extreme weather over western North America (e.g. Knapp *et al.*, 2004). The mechanism highlighted in our study relies primarily on an east–west reorganisation of the storm track and, as such, it might not be as relevant to the North Atlantic where the ocean basin size is smaller. However, it seems particularly relevant to the Southern Ocean, downstream of the Agulhas Front, where similar dynamics might influence the prevalence of Australian blocking patterns.

Acknowledgements

Appendix

Interpretation of anomalous blocking

In section 4, through analysis of the **E** vector divergence, we showed that the sense of the barotropic transient eddy forcing during the positive phase of the KEF index is to reduce the westerly barotropic flow and during these periods blocking frequency is significantly increased. Here, we outline how this result can be well interpreted in terms of the eddy-straining mechanism of barotropic blocking.

Shutts (1983) showed that in the time-mean barotropic eddy enstrophy equation, assuming that the rotational component of the eddy PV flux is largely cancelled by the eddy enstrophy advection term (Marshall and Shutts, 1981; Illari and Marshall, 1983), the residual barotropic PV flux, $\overline{(\mathbf{v}'q')}_*$, is determined by

$$\overline{(\mathbf{v}'q')}_* \cdot \nabla \overline{q} = \overline{F'q'} - r\overline{q'^2}. \tag{A1}$$

Here primes denote deviation from the time mean, $q = f_0 + \zeta + \beta y$ is the barotropic PV (where f_0 is a reference value of the Coriolis parameter and ζ is the relative vorticity), y is the latitude and β the meridional planetary vorticity gradient, F' is the forcing of the barotropic mode by baroclinic instability (which is directly related to transient eddy heat transport), and r^{-1} is a damping time-scale. Since the forcing term $\overline{F'q'}$ is positive

[†]National Centres for Environmental Prediction–National Center for Atmospheric Research.
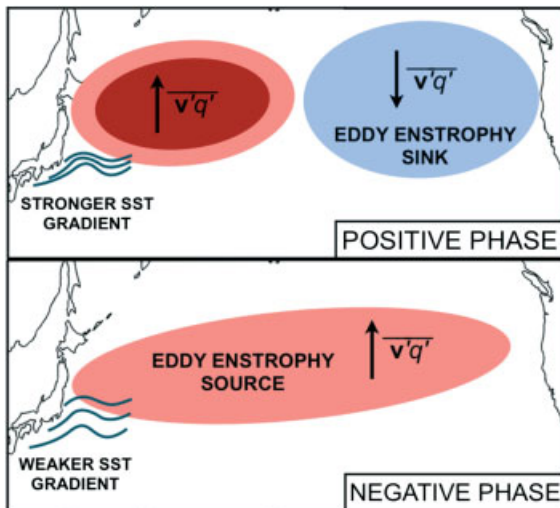
Figure A1. Schematic of the barotropic eddy enstrophy sources/sinks and the associated barotropic potential vorticity fluxes in the positive and negative phases of the KEF. In the positive phase, there is enhanced baroclinic growth in the western Pacific and barotropic dissipation in the eastern Pacific. In the negative phase, the region of baroclinic growth spans the Pacific and the entire region is a net source of barotropic eddy enstrophy (up-gradient flux of barotropic potential vorticity). This leads to enhanced down-gradient barotropic potential vorticity fluxes which act to enhance blocking flows. This figure is available in colour online at wileyonlinelibrary.com/journal/qj

definite, regions where baroclinic instability is large act as *sources* of eddy enstrophy and the eddy PV flux is up-gradient:

$$\overline{(\mathbf{v}'q')}_* . \nabla \overline{q} \approx \overline{F'q'}, \qquad \text{where } \overline{|F'|} \text{ is large.} \qquad (A2)$$

In contrast, regions with little baroclinic eddy growth are net *sinks* of eddy enstrophy and the PV flux is necessarily down-gradient:

$$\overline{(\mathbf{v}'q')}_* . \nabla \overline{q} \approx -r\overline{q'^2}, \qquad \text{where } \overline{|F'|} \text{ is small.} \qquad (A3)$$

This down-gradient flux of PV acts to maintain the PV anomaly of the blocking pattern.

The difference in blocking frequency over the eastern Pacific shown in Figure 8(b) can be interpreted in terms of the barotropic model as follows (also Figure A1). In the negative phase, there is enhanced baroclinic growth but this is confined to the western Pacific region and the eddies become highly barotropic by the time they reach the centre of the Pacific (small $\overline{|F'|}$), consistent with an accelerated lifecycle (e.g. Simmons and Hoskins, 1978). As such, there is increased barotropic dissipation, and hence a sink of barotropic eddy enstrophy in the eastern Pacific. The associated down-gradient barotropic PV fluxes in turn increase the prevalence of blocking patterns. In the positive phase, the baroclinic growth rate is reduced and the eddies take a longer time to become significantly barotropic. As a result, the region of baroclinic growth (large $\overline{|F'|}$), and hence the source of barotropic eddy enstrophy, spans the Pacific and the entire region is a net source of barotropic eddy enstrophy. The eddy barotropic PV flux is therefore upgradient and hence prevents the formation of blocks.

References

Barriopedro D, García-Herrera R, Lupo AR, Hernández E. 2006. A climatology of northern hemisphere blocking. *J. Clim.* **19**: 1042–1063.

Berrisford P, Dee D, Fielding K, Fuentes M, Kållberg P, Kobayashi S, Uppala S. 2009. 'The ERA-Interim archive', ERA Report Series 1. ECMWF: Reading, UK.

Brayshaw DJ, Hoskins BJ, Blackburn M. 2008. The storm-track response to idealized SST perturbations in an aquaplanet GCM. *J. Atmos. Sci.* **65**: 2842–2860.

Bretherton CS, Smith C, Wallace JM. 1992. An intercomparison of methods for finding coupled patterns in climate data. *J. Clim.* **5**: 541–560.

Carrera M, Higgins R, Kousky V. 2004. Downstream weather impacts associated with atmospheric blocking over the northeast pacific. *J. Clim.* **17**: 4823–4839.

Chang EK, Fu Y. 2002. Interdecadal variations in Northern Hemisphere winter storm track intensity. *J. Clim.* **15**: 642–658.

Chen S. 2008. The Kuroshio Extension front from satellite sea surface temperature measurements. *J. Oceanogr.* **64**: 891–897.

Chen TC, Yoon JH. 2002. Interdecadal variation of the North Pacific wintertime blocking. *Mon. Weather Rev.* **130**: 3136–3143.

Chen G, Plumb RA, Lu J. 2010. Sensitivities of zonal mean atmospheric circulation to SST warming in an aquaplanet model. *Geophys. Res. Lett.* **37**: L12701, doi: 10.1029/2010GL043473.

Compo GP, Sardeshmukh PD, Penland C. 2001. Changes of subseasonal variability associated with El Niño. *J. Clim.* **14**: 3356–3374.

Czaja A, Marshall J. 2006. The partitioning of poleward heat transport between the atmosphere and ocean. *J. Atmos. Sci.* **63**: 1498–1511.

Deser C, Alexander MA, Xie SP, Phillips AS. 2010. Sea surface temperature variability: Patterns and mechanisms. *Annu. Rev. Mar. Sci.* **2**: 115–143.

Ducet N, Le Traon PY, Reverdin G. 2000. Global high-resolution mapping of ocean circulation from TOPEX/Poseidon and ERS-1 and-2. *J. Geophys. Res. Oceans* **105**: 19477–19498, doi: 10.1029/2000JC900063.

Duchon CE. 1979. Lanczos filtering in one and two dimensions. *J. Appl. Meteorol.* **18**: 1016–1022.

Frankignoul C, Sennéchael N, Kwon YO, Alexander MA. 2011. Influence of the meridional shifts of the kuroshio and the oyashio extensions on the atmospheric circulation. *J. Clim.* **24**: 762–777.

Green JSA. 1977. The weather during July 1976: Some dynamical considerations of the drought. *Weather* **32**: 120–126.

Hoerling MP, Ting M. 1994. Organization of Extratropical Transients during El Niño. *J. Climate* **7**: 745–766.

Horel JD, Wallace JM. 1981. Planetary-scale atmospheric phenomena associated with the southern oscillation. *Mon. Weather Rev.* **109**: 813–829.

Hoskins BJ, Valdes PJ. 1990. On the existence of storm-tracks. *J. Atmos. Sci.* **47**: 1854–1864.

Hoskins BJ, James IN, White GH. 1983. The shape, propagation and mean-flow interaction of large-scale weather systems. *J. Atmos. Sci.* **40**: 1595–1612.

Hoskins BJ, McIntyre M, Robertson AW. 1985. On the use and significance of isentropic potential vorticity maps. *Q. J. R. Meteorol. Soc.* **111**: 877–946.

Hotta D, Nakamura H. 2011. On the significance of the sensible heat supply from the ocean in the maintenance of the mean baroclinicity along storm tracks. *J. Clim.* **24**: 3377–3401.

Illari L, Marshall JC. 1983. On the interpretation of eddy fluxes during a blocking episode. *J. Atmos. Sci.* **40**: 2232–2242.

Inatsu M, Hoskins BJ. 2004. The zonal asymmetry of the Southern Hemisphere winter storm track. *J. Clim.* **17**: 4882–4892.

Inatsu M, Mukougawa H, Xie SP. 2003. Atmospheric response to zonal variations in midlatitude SST: Transient and stationary eddies and their feedback. *J. Clim.* **16**: 3314–3329.

Joyce TM, Kwon YO, Yu L. 2009. On the relationship between synoptic wintertime atmospheric variability and path shifts in the Gulf Stream and the Kuroshio Extension. *J. Clim.* **22**: 3177–3192.

Kelly KA, Small RJ, Samelson R, Qiu B, Joyce TM, Kwon YO, Cronin MF. 2010. Western boundary currents and frontal air-sea interaction: Gulf Stream and Kuroshio Extension. *J. Clim.* **23**: 5644–5667.

Knapp PA, Soulé PT, Grissino-Mayer HD. 2004. Occurrence of sustained droughts in the interior Pacific Northwest (AD 1733–1980) inferred from tree-ring data. *J. Clim.* **17**: 140–150.

Kwon YO, Deser C. 2007. North Pacific decadal variability in the community climate system model version 2. *J. Clim.* **20**: 2416–2433.

Kwon YO, Alexander MA, Bond NA, Frankignoul C, Nakamura H, Qiu B, Thompson LA. 2010. Role of the Gulf Stream and Kuroshio–Oyashio systems in large-scale atmosphere-ocean interaction: A review. *J. Clim.* **23**: 3249–3281.

Marshall J, Shutts G. 1981. A note on rotational and divergent eddy fluxes. *J. Phys. Oceanogr.* **11**: 1677–1679.

Nakamura H, Sampe T. 2002. Trapping of synoptic-scale disturbances into the North Pacific subtropical jet core in midwinter. *Geophys. Res. Lett.* **29**: 8-1–8-4, doi: 10.1029/2002GL015535.

Nakamura H, Wallace JM. 1990. Observed changes in baroclinic wave activity during the life cycles of low-frequency circulation anomalies. *J. Atmos. Sci.* **47**: 1100–1116.

Nakamura H, Izumi T, Sampe T. 2002. Interannual and decadal modulations recently observed in the Pacific storm track activity and East Asian winter monsoon. *J. Clim.* **15**: 1855–1874.

Nakamura H, Sampe T, Tanimoto Y, Shimpo A. 2004. Observed associations among storm tracks, jet streams and midlatitude oceanic fronts. *Geophys. Monogr. AGU* **147**: 329–345.

Nakamura H, Sampe T, Goto A, Ohfuchi W, Xie SP. 2008. On the importance of midlatitude oceanic frontal zones for the mean state and dominant variability in the tropospheric circulation. *Geophys. Res. Lett.* **35**: L15709, doi: 10.1029/2008GL034010.

Nakamura H, Nishina A, Minobe S. 2012. Response of storm tracks to bimodal Kuroshio path states south of Japan. *J. Clim.* **25**: 7772–7779.

Ogawa F, Nakamura H, Nishii K, Miyasaka T, Kuwano-Yoshida A. 2012. Dependence of the climatological axial latitudes of the tropospheric westerlies and storm tracks on the latitude of an extratropical oceanic front. *Geophys. Res. Lett.* **39**: L05804, doi: 10.1029/2011GL049922.

Orlanski I. 2005. A new look at the pacific storm track variability: Sensitivity to tropical ssts and to upstream seeding. *J. Atmos. Sci.* **62**: 1367–1390.

Qiu B, Chen S. 2005. Variability of the Kuroshio Extension jet, recirculation gyre, and mesoscale eddies on decadal time scales. *J. Phys. Oceanogr.* **35**: 2090−2103.

Qiu B, Schneider N, Chen S. 2007. Coupled decadal variability in the north pacific: An observationally constrained idealized model. *J. Clim.* **20**: 3602−3620.

Renwick JA, Wallace JM. 1996. Relationships between North Pacific wintertime blocking, El Niño, and the PNA pattern. *Mon. Weather Rev.* **124**: 2071−2076.

Reynolds RW, Smith TM. 1994. Improved global sea surface temperature analyses using optimum interpolation. *J. Clim.* **7**: 929−948.

Reynolds RW, Smith TM, Liu C, Chelton DB, Casey KS, Schlax MG. 2007. Daily high-resolution-blended analyses for sea surface temperature. *J. Clim.* **20**: 5473−5496.

Robinson WA. 2000. A baroclinic mechanism for the eddy feedback on the zonal index. *J. Atmos. Sci.* **57**: 415−422.

Robinson WA. 2006. On the self-maintenance of midlatitude jets. *J. Atmos. Sci.* **63**: 2109−2122.

Sampe T, Hisashi N, Atsushi G, Wataru O. 2010. Significance of a Midlatitude SST Frontal Zone in the Formation of a Storm Track and an Eddy-Driven Westerly Jet. *J. Climate* **23**: 1793−1814.

Sasaki YN, Minobe S, Schneider N. 2013. Decadal response of the kuroshio extension jet to rossby waves: Observation and thin-jet theory. *J. Phys. Oceanogr.* **43**: 442−456.

Seager R, Harnik N, Robinson W, Kushnir Y, Ting M, Huang HP, Velez J. 2005. Mechanisms of enso-forcing of hemispherically symmetric precipitation variability. *Q. J. R. Meteorol. Soc.* **131**: 1501−1527.

Sheldon L, Czaja A. 2014. Seasonal and interannual variability of an index of deep atmospheric convection over western boundary currents. *Q. J. R. Meteorol. Soc.* **140**: 22−30.

Shutts G. 1983. The propagation of eddies in diffluent jetstreams: Eddy vorticity forcing of blockingflow fields. *Q. J. R. Meteorol. Soc.* **109**: 737−761.

Shutts G. 1986. A case study of eddy forcing during an atlantic blocking episode. *Adv. Geophys.* **29**: 135−162.

Simmons AJ, Hoskins BJ. 1978. The life cycles of some nonlinear baroclinic waves. *J. Atmos. Sci.* **35**: 414−432.

Taguchi B, Nakamura H, Nonaka M, Xie SP. 2009. Influences of the Kuroshio/Oyashio Extensions on air-sea heat exchanges and storm-track activity as revealed in regional atmospheric model simulations for the 2003/04 cold season. *J. Clim.* **22**: 6536−6560.

Taguchi B, Nakamura H, Nonaka M, Komori N, Kuwano-Yoshida A, Takaya K, Goto A. 2012. Seasonal evolutions of atmospheric response to decadal SST anomalies in the North Pacific subarctic frontal zone: Observations and a coupled model simulation. *J. Clim.* **25**: 111−139.

Tanimoto Y, Nakamura H, Kagimoto T, Yamane S. 2003. An active role of extratropical sea surface temperature anomalies in determining anomalous turbulent heat flux. *J. Geophys. Res.* **108**: 3304, doi: 10.1029/2002JC001750.

Tibaldi S, Molteni F. 1990. On the operational predictability of blocking. *Tellus A* **42**: 343−365.

Trenberth KE. 1984. Some effects of finite sample size and persistence on meteorological statistics. Part I: Autocorrelations. *Mon. Weather Rev.* **112**: 2359−2368.

Trenberth KE, Hurrell JW. 1994. Decadal atmosphere-ocean variations in the pacific. *Clim. Dyn.* **9**: 303−319.

Trenberth KE, Branstator GW, Karoly D, Kumar A, Lau NC, Ropelewski C. 1998. Progress during toga in understanding and modeling global teleconnections associated with tropical sea surface temperatures. *J. Geophys. Res.: Oceans* **103**: 14291−14324, doi: 10.1029/97JC01444.

Woollings T, Hoskins B, Blackburn M, Hassell D, Hodges K. 2010. Storm track sensitivity to sea surface temperature resolution in a regional atmosphere model. *Clim. Dyn.* **35**: 341−353.

Yu L, Jin X, Weller R. 2008. 'Multidecade global flux datasets from the Objectively Analyzed Air-sea Fluxes (OAFlux) Project: Latent and sensible heat fluxes, ocean evaporation, and related surface meteorological variables'. OAFlux Project Technical report OA-2008-01. Woods Hole Oceanographic Institution: Woods Hole, MA.

Zhang Y, Wallace JM, Battisti DS. 1997. ENSO-like interdecadal variability: 1900−1993. *J. Clim.* **10**: 1004−1020.